Reference Trajectory Reshaping Optimization and Control of Robotic Exoskeletons for Human–Robot Co-Manipulation

Xiaoyu Wu, Zhijun Li, *Senior Member, IEEE*, Zhen Kan, and Hongbo Gao

***Abstract*—For human–robot co-manipulation by robotic exoskeletons, the interaction forces provide a communication channel through which the human and the robot can coordinate their actions. In this article, an optimization approach for reshaping the physical interactive trajectory is presented in the co-manipulation tasks, which combines impedance control to enable the human to adjust both the desired and the actual trajectories of the robot. Different from previous studies, the proposed method significantly reshapes the desired trajectory during physical human–robot interaction (pHRI) based on force feedback, without requiring constant human guidance. The proposed scheme first formulates a quadratically constrained programming problem, which is then solved by neural dynamics optimization to obtain a smooth and minimal-energy trajectory similar to the natural human movement. Then, we propose an adaptive neural-network controller based on the barrier Lyapunov function (BLF), which enables the robot to handle the uncertain dynamics and the joint space constraints directly. To validate the proposed method, we perform experiments on the exoskeleton robot with human operators for co-manipulation tasks. The experimental results demonstrate that the proposed controller could complete the co-manipulation tasks effectively.**

***Index Terms*—Optimized trajectory, physical human–robot interaction (pHRI), reference trajectory reshaping, robotic exoskeleton.**

I. Introduction

THE EXOSKELETON robots are being increasingly used in medical care to assist physically disabled people, deliver consistent and repeatable movement therapy, and improve endurance and safety in rehabilitation [1]–[3]. Compared with the traditional rehabilitation methods, it has been proven in [4]–[6] that exoskeleton robots are more efficient and effective in dealing with repetitive movement. Recently, an assist-as-needed (AAN) control has been studied for upper-limb robotics rehabilitation. In [7], a minimal AAN controller, which utilizes force estimation to independently determine subject capability, had been proposed. In [8], a novel AAN controller based on the optimal control framework for physical human–robot interaction (pHRI) had been developed. However, such an interaction between the operator and the upper-limb exoskeleton would bring new challenges. One of the most critical issues in robotic exoskeleton control is how to make humans modulate the desired trajectory of the robot so that the human could cooperate with the robot actively. In co-manipulation, it is desirable that the robotic exoskeleton provide natural and smooth movement that resembles a human's motion, rather than trajectories that are hard for humans to follow.

When considering the human–robot co-manipulation tasks, the methods based on classical impedance control [9] have shown a few drawbacks, especially in the initial and the end phases. As indicated in [10], the fixed damping parameter could result in inefficient co-manipulation. The robot with low damping could be dangerous to the operator, as the robotic system can become unstable and cause collisions with human when operating inappropriately. On the contrary, if the damping is set high, the robot could be difficult to manipulate, thus restricting human movement. In fact, it is difficult to solve this problem in the context of pHRI since the human operator, acting as the environment, has variable stiffness. Therefore, variable impedance control has been introduced, and several works have been accomplished. In [11], the variable impedance control was realized by choosing the virtual damping coefficient in a certain range according to the end-effector's velocity. In [12]–[14], a method of online impedance coefficients adjustment based on real-time estimation of human-arm stiffness was also presented. In [15], the variable damping parameters were studied and optimized by minimizing the selected cost function. Recently, in [16] and [17], it was suggested that the virtual impedance coefficient could be adjusted by human intention to guarantee better pHRI. These methods contribute to developing natural, compliant, and safe robotic behavior, and allow for effectively completing co-manipulation tasks. However, impedance control can only allow the human to adjust the actual trajectory of the robot, rather than interacting with the desired trajectory of the robot, which will lead to more human efforts to modulate the robot's behavior, or to produce less efficient human–robot collaboration.

Manuscript received February 3, 2019; revised May 19, 2019 and July 20, 2019; accepted July 24, 2019. Date of publication August 30, 2019; date of current version July 10, 2020. This work was supported in part by the National Natural Science Foundation of China under Grant 61573147, Grant 61625303, and Grant 61751310, in part by the National Key Research and Development Program of China under Grant 2018YFC2001600, and in part by the Anhui Science and Technology Major Program under Grant 17030901029. This article was recommended by Associate Editor Z. Ju. *(Corresponding author: Zhijun Li.)*

The authors are with the Department of Automation, University of Science and Technology of China, Hefei 230060, China (e-mail: zjli@ieee.org).

Color versions of one or more of the figures in this article are available online at http://ieeexplore.ieee.org.

Digital Object Identifier 10.1109/TCYB.2019.2933019

Consequently, the extension of impedance control has been developed to allow the robot to move along the desired trajectory of the human [16], [18]. In these methods, the human, as a master, guides the interaction and generates the desired trajectory, while the robot acts as a follower to estimate the human motion intentions. Since the robot is guided by the human, it is unable to intervene meaningfully toward achieving the goal or accomplishing the task, thus restricting the collaborations. Alternatively, a shared control method for co-manipulation has been proposed, in which the human and the robot can exchange the roles of master and follower autonomously [19]–[21]. Both the human and the robot can make contributions to accomplishing the task, and the autonomous level of the robot is adjusted according to human efforts. Although the robot can now make a meaningful contribution to the co-manipulation task, we observe that the human still cannot directly change the robot's desired trajectory during pHRI. Therefore, this article is motivated to propose a method by combining the benefits of the trajectory redesign and shared control. In this method, haptic interactions act as a bidirectional information exchange in which task-related modifications are physically transmitted to the robot, while the force feedback of the robot notifies the human of the present desired trajectory.

In this article, a framework of physical interactive online trajectory reshaping optimization for human–robot co-manipulation is proposed, which allows the human to interact with the desired and the actual trajectories of the robot simultaneously. In the context of pHRI, the human operator can not only constantly alter or reshape the future part of the robot's desired trajectory but also experiences the compliance rendered by the impedance controller, as is illustrated in Fig. 1. Since the human does not continue to guide the robot, after a certain time interval, the reshaped trajectory can return to the original desired trajectory, and so the robot can also contribute to the completion of the collaborative task. The proposed approach is designed for applications where the robot's behavior is coupled with a real or virtual environment and can be modified by the human operator via physical interactions. First, the human operator exerts the interactive force, based on which optimal trajectory reshaping is explored to find a smooth and optimized trajectory similar to the natural human motion. Second, the robot's motion control to realize the comfortable and safe interaction with the human should be designed, thereby facilitating the accomplishment of the co-manipulation tasks.

To ensure the safety of the operator during pHRI, various physical constraints exist in robotic systems, such as safety specifications and physical limits [22], [23]. Indeed, the maximum range of the joint position of a robotic manipulator is constrained by its physical configuration, which should be carefully taken into account in control design. Many techniques have been studied to deal with such a constraint in various mechanical systems. In [24], a robust adaptive multi-estimation scheme was designed for robot manipulators with uncertainty. In [25], a method of reference speed governor for tracking control under system nonlinearity and state constraints was presented. In [26], a barrier Lyapunov function

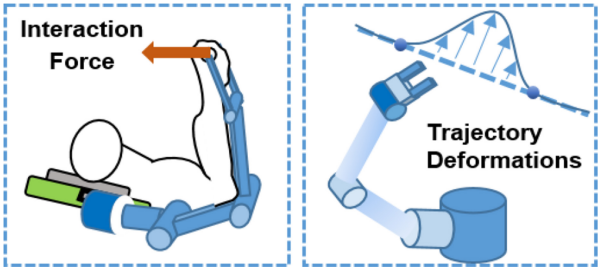

Fig. 1. Task model for robotic exoskeleton with pHRI.

(BLF) was applied to handle the constraints of the joint position in robotic systems. In [27], the control design for output constraints of single-input–single-output (SISO) nonlinear systems was developed. In [28], a BLF was applied to solve the time-varying constraints in nonlinear systems. In [29], a new type of integral BLF controller was developed to solve the state constraint existing in the nonlinear system. In the above-mentioned results, it has been proved that BLF is a feasible and reliable approach for controlling a robotic system with a joint constraint. However, these works do not take into account the state constraints of the system in the context of pHRI (e.g., reducing the potential motion conflicts between the human operator and the robotic exoskeleton in the co-manipulation tasks). Therefore, we propose an adaptive neural-network controller based on BLF to improve tracking performance. A BLF can be used to deal with certain physical constraints while the adaptive neural network can be used in the estimation of unknown parameters in the robotic system model.

In this article, an optimization approach for physical interactive trajectory reshaping in co-manipulation tasks is proposed, which is combined with an adaptive controller. First, we derive accurate constraints to ensure that the proposed controller is compatible with trajectory reshaping, and a quadratically constrained programming problem is formulated, which is solved via the neural dynamics optimization to obtain a smooth and optimal shape similar to the natural human movement. Second, an adaptive neural-network controller based on BLF is designed, which enables the robot to keep the tracking errors, satisfying the constraints and handling the uncertain dynamics. To verify the proposed method, we perform experiments where the co-manipulation task of the human operator is to carry an object with the assistance of the robot. Finally, we evaluate the online trajectory reshaping optimization and control by carrying out the human–robot experiments on a robotic exoskeleton. The results show that the designed method can result in better performance with less control effort from the human.

II. Problem Formulation and Preparation

Consider an upper exoskeleton robot with n joints (its interaction model with human subjects is shown in Fig. 1) according to the Euler–Lagrange dynamics

$$M(q)\ddot{q} + C(q,\dot{q})\dot{q} + M_g(q) + M_v(\dot{q}) + f_{\text{dis}} = \tau + \tau_e(t) \quad (1)$$

where $q \in \mathbb{R}^n$ represents the generalized coordinates of joint position, $\tau \in \mathbb{R}^n$ represents the joint torque vector (i.e., the

control input), $\tau_e \in \mathbb{R}^n$ represents the torque generated from the interaction with the environment (or human), $M(q) \in \mathbb{R}^{n\times n}$ denotes the symmetric and positive-definite inertia matrix, $C(q,\dot{q}) \in \mathbb{R}^{n\times n}$ denotes the Coriolis and centrifugal forces, $M_g(q) \in \mathbb{R}^n$ denotes the gravitational components of the human-exoskeleton couple, $M_v(\dot{q}) \in \mathbb{R}^n$ is the viscous complex between human and exoskeleton due to the damping in the musculotendon, and $f_{\text{dis}} \in \mathbb{R}^n$ represents the external disturbances. The terms $M(q)$, $C(q,\dot{q})$, $M_g(q)$, and $M_v(\dot{q})$ include various dynamic uncertainties.

Considering the position of the exoskeleton end-effector in Cartesian space and its kinematics, the joint space can be transformed into the task Cartesian space via $x = \Omega(q)$ and $\dot{x} = J(q)\dot{q}$, where $\Omega(\cdot) \in \mathbb{R}^n \to \mathbb{R}^m$ is a nonlinear transformation that describes the relationship between the Cartesian space and the joint space, and $J(q)$ is a Jacobian matrix from the joint space to the Cartesian space. According to (1), let $x_1 = [q_1, q_2, q_3, \ldots, q_n]^T, x_2 = [\dot{q}_1, \dot{q}_2, \dot{q}_3, \ldots, \dot{q}_n]^T$, where x_1 and x_2 represent the actual trajectory and the actual velocity, respectively. It is necessary to derive a controller that enables the joint variable x_1 to keep tracking the reference path x_r, even in the presence of the interaction force. Moveover, the closed-loop states are required to be bounded and satisfy the constraint that $|x_{1,i}(t)| < k_{c_i}, i = 1, 2, \ldots, n, \forall t > 0$.

Property 1 [30]: The matrix $\dot{M}(q) - 2C(q,\dot{q})$ is skew-symmetric.

Property 2 [31]: The inverse of matrix $M(q)$ exists, and $M^{-1}(q)$ is positive definite and bounded, that is, $\|M^{-1}(q)\| < \alpha_{M^{-1}}$, where $\alpha_{M^{-1}}$ is a positive constant.

Property 3: Since the exact dynamics model in (1) may not be available beforehand, the unknown nonlinear function in the uncertain MIMO system can be approximated by the adoption of the Gaussian radial basis function neural network (RBFNN). Consider a continuous function $f(Z) : \mathbb{R}^q \longrightarrow \mathbb{R}$, which can be approximated by using the RBFNN as

$$f_n(Z) = W^T S(Z) \tag{2}$$

where $Z \in \Omega \subset \mathbb{R}^q$ denotes the input vector of the RBFNN, and $W = [w_1, w_2, \ldots, w_l]^T \in \mathbb{R}^l$ are the weight vectors of the neural network. In (2), $S(Z) = [S_1(Z), S_2(Z), \ldots, S_l(Z)]^T$ denotes the basis function of the Gaussian RBFNN, which can be defined as

$$S_j(Z) = \exp\left[\frac{-(Z-\sigma_j)^T(Z-\sigma_j)}{\eta_j^2}\right], j = 1, 2, \ldots, l \tag{3}$$

where l is the number of nodes in the hidden layer of the network, σ_j is the center, and η_j is the width of the neural cell. Based on the definition of $S(Z)$, it is known that $S(Z)$ can be upper bounded by a positive constant ζ, that is

$$\|S(Z)\| \le \zeta. \tag{4}$$

If the node number l is large enough, any smooth continuous function can be approximated to any degree in the following form:

$$f(Z) = W^{*T} S(Z) + \epsilon, \forall Z \in \Omega_z \tag{5}$$

where $\Omega_z \subset \mathbb{R}^q$ denotes a compact set; ϵ denotes the approximation error of the RBFNN which has a positive unknown upper bound ϵ_N, that is, $|\epsilon| \le \epsilon_N$; and W^* is an optimal weight, which can be obtained by

$$W^* = \arg\min_{W\in\mathbb{R}^l}\{\sup_{Z\in\Omega_z}|f(Z) - W^T S(Z)|\}. \tag{6}$$

Lemma 1 [32]: Consider a continuous and positive-definite Lyapunov function $V(x)$ which satisfies $\phi_1(\|x\|) \le V(x) \le \phi_2(\|x\|)$, such that $\dot{V}(x) \le -\phi V(x) + \varepsilon$, where $\phi_1, \phi_2 : \mathbb{R}^n \to \mathbb{R}$ are the functions, and ϕ and ε are the positive constants. Then, the solution of the Lyapunov function $x(t)$ is uniformly bounded.

Lemma 2 [33]: For any given positive constant k_d, let $\mathcal{Z} := \{z_1 \in \mathbb{R} : -k_d < z_1 < k_d\} \subset \mathbb{R}$ and $\mathcal{N} := \mathbb{R}^l \times \mathcal{Z} \subset \mathbb{R}^{l+1}$ be the open sets. Consider the following system:

$$\dot{z} = g(t, z)$$

where $z := [z_2, z_1]^T \subset \mathcal{N}(z_2 \in \mathbb{R}^l)$ and $g : \mathbb{R}^+ \times \mathcal{Z} \subset \mathcal{N} \longrightarrow \mathbb{R}^{l+1}$ are uniform in t, locally Lipschitz in z, and piecewise continuous on $\mathbb{R}^+ \times \mathcal{N}$. Two functions $U : \mathbb{R}^l \times \mathbb{R}^+ \longrightarrow \mathbb{R}^+$ and $V_1 : \mathcal{Z} \longrightarrow \mathbb{R}^+$ are defined, which are positive definite and continuously differentiable in their respective fields, and then we have

$$V_1(z_1) \longrightarrow \infty \quad \text{as} \quad |z_1| \longrightarrow k_d$$
$$\delta_1(\|z_2\|) \le U(z_2, t) \le \delta_2(\|z_2\|)$$

where δ_1 and δ_2 are class K_∞ functions. Define $V(z) := V_1(z_1, t) + U(z_2)$, and $z_1(0) \in \mathcal{Z} \in (-k_d, k_d)$. $z_1(t)$ will remain in the open set $z_1 \in (-k_d, k_d), \forall t \in [0, +\infty)$ if the inequality satisfies

$$\dot{V} = \frac{\partial V}{\partial z} g \le -\kappa V + Z$$

where κ and Z are the positive constants. As shown in Fig. 3, z is bounded and $z(t) \in \mathcal{Z}, \forall t \in [0, +\infty)$.

III. Trajectory Reshaping Optimization

In this section, the human–robot interaction is used to reshape the robot's desired trajectory and obtain an optimal reference trajectory. We will explain how the reference trajectory is deformed and optimized and how the corresponding controller is designed to ensure the stability of the robotic system with nonlinearities, uncertainties, and the changing human–robot interactions. The control framework is shown in Fig. 2.

A. Reference Trajectory Reshaping

The dynamics of the robot can be rewritten in the Cartesian space as

$$M_x(x)\ddot{x} + C_x(x,\dot{x})\dot{x} + G_x(x,\dot{x}) + F_{\text{dis}}(t) = f + F_h \tag{7}$$

where $M_x = J^{-T}M(q)J^{-1}, C_x = J^{-T}(-M(q)J^{-1}\dot{J} + C(q,\dot{q}))J^{-1}, G_x = J^{-T}(M_g(q) + M_v(\dot{q})), F_{\text{dis}} = J^{-T}f_{\text{dis}}, f = J^{-T}\tau$, and $F_h = J^{-T}\tau_e$.

An impedance model with virtual force is considered as

$$M(\ddot{x} - \ddot{x}_d) + D(\dot{x} - \dot{x}_d) + K(x - x_d) = F_h \tag{8}$$

where $x \in \mathbb{R}^n$ denotes the position of the exoskeleton end-effector; $x_d \in \mathbb{R}^n$ denotes the desired position; M, D,

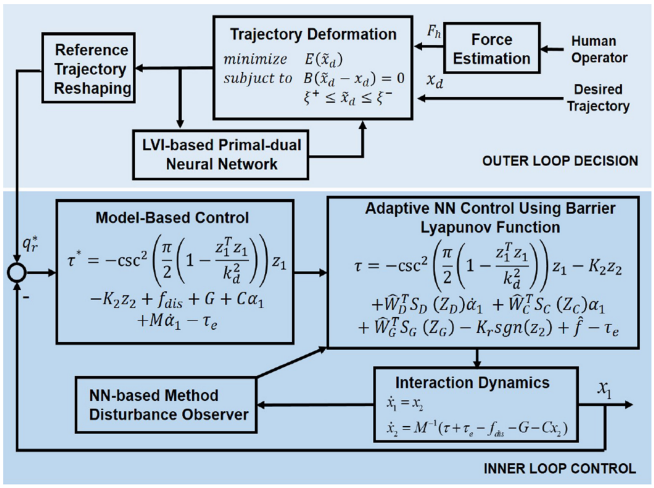

Fig. 2. Block diagram of human–robot interaction scheme, including the outer-loop decision and the inner-loop control.

and K represent the inertia, damping, and stiffness matrix, respectively; and F_h denotes the interaction force. Using the aforementioned model, the relationship between the external force and the task error can be adjusted, and x_d can also be the initial desired trajectory. It is well known that the input of the human not only influences the current state of the robot via an impedance controller but also affects the future behavior of the robot through trajectory reshaping. Specifically, the desired trajectory is reinitialized to x_d^*, if pHRI does not occur, that is, $F_h = \mathbf{0}, x_d(t) = x_d^*(t)$. Whenever there is a physical interaction between the human and the robot, the robot's desired trajectory is modified or "reshaped," and using x_d to represent this deformation, while the time required to achieve this co-manipulation task will not change during trajectory reshaping. Since x_d is continually modified with respect to f_h during the interactive process, it is referred to as physically interactive trajectory reshaping.

For the segment of trajectory reshaping, let us define t_i and t_f as the initial and end time, respectively; thus, $\Delta t = t_f - t_i$ as the duration of the reshaped trajectory. We define $\tilde{x}_d$ as the part of the desired trajectory within human interaction. Once $\tilde{x}_d$ is determined, x_d is then updated as $x_d(t) = \tilde{x}_d(t)$ over the interval $t \in [t_i, t_f]$. After time t_f, since the humans do not continue to interact with the future trajectory, the robot then tracks the original desired trajectory x_d^*. We assume that $X_d^s(t)$ is a family of trajectories which consists of numerous possible, smooth trajectories deformation, and it can be re-expressed as

$$X_d^s = x_d(t) + s\Phi(t) \quad \forall t \in \left[t_i, t_f\right]. \tag{9}$$

Define $X_d^1 = \tilde{x}_d$, that is, the curve $X_d(s,t)$ for $s = 1$ as the optimal trajectory reshaping. Then, we have $\tilde{x}_d(t) = x_d(t) + \Phi(t)$, where Φ is a vector field along x_d. In addition, it is known that $\tilde{x}_d(t) = x_d(t)$ and $\dot{\tilde{x}}_d(t) = \dot{x}_d(t)$ at the start time t_i and the end time t_f of the reshaped trajectory.

In particular, we first consider an element in the vector $x_d \in \mathbb{R}^n$. Other n-1-dimensional elements can be extrapolated the same way. Since the time duration of the part of x_d during the pHRI is $t_f - t_i$, the number of waypoints along x_d and $\tilde{x}_d$ is defined as $N = [(t_f - t_i)/\delta] + 1$, where δ is the time interval between consecutive waypoints. We can obtain that x_d and $\tilde{x}_d$ are the vectors of length N. In this article, we minimize the energy of the trajectory to obtain the human's intended desired trajectory [36]

$$E(\tilde{x}_d) = E(x_d) + (\tilde{x}_d - x_d)^T\left(-\hat{F}_h\right) + \frac{1}{2\alpha}(\tilde{x}_d - x_d)^T R(\tilde{x}_d - x_d) \tag{10}$$

where $E(x_d)$ is the energy of the undeformed trajectory, x_d is the segment of the desired trajectory, and $\tilde{x}_d$ is the reshaped x_d with the same dual representations. We suppose that the future applied force will always be equal to the initial input force

$$\hat{F}_h = \vec{1} f_h(t_i), \hat{F}_h \in \mathbb{R}^N \tag{11}$$

where $\vec{1} \in R^N$ represents a vector of all ones, f_h is the force exerted by the human at initial time t_i, and N denotes the number of waypoints along x_d or $\tilde{x}_d$. According to [35], a minimum-jerk model can represent the trajectory of human motion accurately. Thus, to ensure that the obtained trajectory reshaping is natural to the human, A is defined as a finite difference matrix $R = A^T A, R \in \mathbb{R}^{N\times N}$

$$A = \begin{pmatrix} 1 & 0 & 0 & & 0 \\ -3 & 1 & 0 & & 0 \\ 3 & -3 & 1 & \cdots & 0 \\ -1 & 3 & -3 & & 0 \\ 0 & -1 & 3 & & 0 \\ & \vdots & & \ddots & \vdots \\ 0 & 0 & 0 & & 1 \\ 0 & 0 & 0 & & -3 \\ 0 & 0 & 0 & \cdots & 3 \\ 0 & 0 & 0 & & -1 \end{pmatrix}, A \in \mathbb{R}^{(N+3)\times N}. \tag{12}$$

According to [36], the third term in (10) indicates the minimum energy associated with the natural trajectory of Φ, so we have

$$\tilde{x}_d(t) = x_d(t) + \Phi(t) \quad \forall t \in \left[\tau_i, \tau_f\right] \tag{13}$$

where $\Phi(t)$ is the deformation of the initial trajectory $x_d(t)$, which is used to generate $\tilde{x}_d(t)$. The optimization of the energy function needs to satisfy the constraint

$$B(\tilde{x}_d - x_d) = 0 \tag{14}$$

where the matrix $B \in \mathbb{R}^{4\times N}$

$$B = \begin{pmatrix} 1 & 0 & 0 & \cdots & 0 & 0 & 0 \\ 0 & 1 & 0 & \cdots & 0 & 0 & 0 \\ 0 & 0 & 0 & \cdots & 0 & 1 & 0 \\ 0 & 0 & 0 & \cdots & 0 & 0 & 1 \end{pmatrix}. \tag{15}$$

Intuitively, the constraint (14) ensures that the first two and last two points of $\tilde{x}_d$ are the same as x_d, that is, the four constraints corresponding to the initial and final values of the reshaped trajectory mentioned above. Combining (10) and (14), the optimization problem is described as

$$\begin{aligned} &\text{minimize} \quad E(\tilde{x}_d) \\ &\text{subject to} \quad B(\tilde{x}_d - x_d) = 0. \end{aligned} \tag{16}$$

The solution of (16) provides a "best" reshaped $\tilde{x}_d$. As demonstrated in [34], the optimization problem (16) can be handled by the method of linear variational inequality-based primal–dual neural network (LVI-PDNN). Therefore, the optimization problem in (16) can be reformulated as

$$E(\tilde{x}_d) = \frac{1}{2\alpha}\tilde{x}_d^T R\tilde{x}_d - \left(\frac{1}{\alpha}x_d^T R + \hat{F}_h^T\right)\tilde{x}_d + E(x_d) + x_d^T\hat{F}_h + \frac{1}{2\alpha}x_d^T R x_d. \tag{17}$$

Since the last three terms on the right-hand side of (17) are independent of $\tilde{x}_d$, the optimization can be rewritten as

$$\begin{aligned} \text{minimize} \quad & \frac{1}{2\alpha}\tilde{x}_d^T R\tilde{x}_d - \left(\frac{1}{\alpha}x_d^T R + \hat{F}_h^T\right)\tilde{x}_d \\ \text{subject to} \quad & B(\tilde{x}_d - x_d) = 0. \end{aligned} \tag{18}$$

Since the large values of $\tilde{x}_d$ may cause potential mechanical damage when the robotic exoskeleton is close to its limits, physical limits of the robotic exoskeleton should be taken into account. Therefore, the optimization problem of trajectory reshaping can be finally rewritten in a quadratic form

$$\text{minimize} \quad \frac{1}{2}\tilde{x}_d^T W\tilde{x}_d + c^T\tilde{x}_d \tag{19}$$

$$\text{subject to} \quad B\tilde{x}_d = b \tag{20}$$

$$\xi^- \le \tilde{x}_d \le \xi^+ \tag{21}$$

$$\text{with} \quad W \coloneqq \frac{R}{\alpha}, c \coloneqq -\left(\frac{1}{\alpha}Rx_d + \hat{F}_h\right), b = Bx_d$$

where $\tilde{x}_d \in \mathbb{R}^N$ is the decision variable vector, $W \in \mathbb{R}^{N\times N}$ and $B \in \mathbb{R}^{4\times N}$ are the coefficient matrix, and $c \in \mathbb{R}^N$ and $b \in \mathbb{R}^4$ are the coefficient vectors. The performance index (19) is simplified as (16). The equality constraint (20) indicates a linear relationship between x_d and $\tilde{x}_d$ at the initial time. The bound constraints $\xi^+ \in \mathbb{R}^N$ and $\xi^- \in \mathbb{R}^N$ in (21) are used to ensure all positions within the mechanical limits of the system. Moreover, it should be noted that almost all parameters in (19)–(21) are state dependent and time varying, which demands a real-time solution of the energy-related optimization.

B. Neural Dynamics Optimization

To improve the effectiveness of the QP (19)–(21) online solution, the method of LVI-PDNN is used as the QP real-time solver [34]. First, by the duality theory [40], the dual problem of the primal QP problem (19)–(21) can be derived by using the Lagrangian multiplier of each constraint as the dual decision variable in (20) and (21). Moreover, elegant processing of canceling the dual decision variable for the bound constraint (21) can be used to simplify the QP solver. Then, we define the augmented primal–dual decision variable v and its bounds $v^{\pm}$, respectively, as

$$v = \begin{bmatrix}\tilde{x}_d \\ \tilde{y}_d\end{bmatrix}, v^+ = \begin{bmatrix}\xi^+ \\ \varpi 1_v\end{bmatrix}, v^- = \begin{bmatrix}\xi^- \\ -\varpi 1_v\end{bmatrix} \in \mathbb{R}^{n+m} \tag{22}$$

where $1_v \coloneqq [1, \ldots, 1]^T$ is a vector of ones with appropriate dimensions, and $\varpi \gg 0$ is large enough to replace $+\infty$ for the purpose of implementation. We define the convex set Ω as $\Omega = \{v \in \mathbb{R}^{N+m} \mid v^- \le v \le v^+ \subset \mathbb{R}^{N+m}\}$. The definitions of the coefficients H and μ are as follows:

$$H = \begin{bmatrix}W & -B \\ B & 0\end{bmatrix} \in \mathbb{R}^{(N+m)\times(N+m)}, \mu = \begin{bmatrix}c \\ -b\end{bmatrix} \in \mathbb{R}^{N+m}. \tag{23}$$

Theorem 1 [38] (QP Duality): For the primal QP problem described in (19)–(21), we can derive its dual QP problem as

$$\begin{aligned} \text{minimize} \quad & -\frac{1}{2}\tilde{x}_d^T W\tilde{x}_d + \tilde{y}_d^T b + \beta^{-T}\xi^- - \beta^{+T}\xi^+ \\ \text{subject to} \quad & W\tilde{x}_d + c - B^T\tilde{y}_d - \beta^- + \beta^+ = 0 \\ & \tilde{y}_d \quad \text{unrestricted}, \beta^- \ge 0, \beta^+ \ge 0 \end{aligned}$$

where corresponding to the equality constraint (20) is the dual decision vector $\tilde{y}_d \in \mathbb{R}^m$; corresponding to the left part of the bound constraint (21) is the dual decision vector $\beta^- \in \mathbb{R}^N$, that is, $\xi^- \le \tilde{x}_d \in \mathbb{R}^N$; and corresponding to the right part of the bound constraint (21) is $\beta^+ \in \mathbb{R}^N$, that is, $\tilde{x}_d \le \xi^+ \in \mathbb{R}^N$.

Theorem 2 [39] (QP-LVI Conversion): The QP problem (19)–(21) can be transformed into the following LVI problem, which aims to obtain a primal–dual equilibrium vector $v^* \in \Omega$ such that

$$(v - v^*)^T(Hv^* + \mu) \ge 0, \forall v \in \Omega. \tag{24}$$

Note that the above-mentioned LVI inequality (24) can be written in the form of the following piecewise-linear equations:

$$P_\Omega(v - (Hv + \mu)) - v = 0 \tag{25}$$

where $P_\Omega(\cdot) : \mathbb{R}^{n+m} \to \Omega$ denotes a projection operator onto Ω, where the ith element of $P_\Omega(v)$ is

$$P_\Omega(v) = \begin{cases} v_i^-, & \text{if } v_i < v_i^- \\ v_i, & \text{if } v_i^- \le v_i \le v_i^+ \\ v_i^+, & \text{if } v_i > v_i^+. \end{cases} \tag{26}$$

The following dynamics for the LVI-PDNN is adopted to deal with the LVI (25) and QP (19)–(21) problem as:

$$\dot{v} = \lambda\left(I + H^T\right)(P_\Omega(v - (Hv + \mu)) - v) \tag{27}$$

where λ is a positive constant for scaling the convergence rate of the neural network.

Theorem 3 [39] (LVI-PDNN Convergence): Suppose there exists an optimal solution v^* to the QP problem (19)–(21). The state vector $v(t)$ of LVI-PDNN (27), beginning with any initial state $v(0)$, will converge to the equilibrium point v^*, where the optimal solution $\tilde{x}_d^*$ of the QP problem (19)–(21) is composed of the first n elements. In addition, if there exits a constant ρ satisfying $\|v - P_\Omega(v - (Hv + \mu))\|_2^2 \ge \rho\|v - v^*\|_2^2$, then the exponential convergence can be obtained by the LVI-PDNN (27) with a convergence rate $\lambda\rho$.

Finally, it is worth comparing the computational complexity of the above neural-network solver with the traditional numerical algorithm, and the results are given in the following remarks.

Remark 1: In general, quadratic programming can be employed to solve (19). However, the minimum computational cost of a QP numerical algorithm is generally

proportional to the dimension of the decision vector. For the traditional quadratic programming methods, such as the interior point algorithm, it is necessary to repeatedly calculate the Hessian matrix of Lagrangian. Considering the time-varying characteristics of the QP problem in (19) and the online-solution requirements, the numerical algorithm includes $O(N^4 + N + (N + m)N^2 + (2N + m)^3)$ operations, while the proposed PDNN method includes $O(7(N + m) + 2(N + m)^2)$ operations. In contrast, the LVI-PDNN method is more effective for online optimization of real-time robot systems. To calculate the control increment $\tilde{x}_d$ in (19), the computational time of the LVI-PDNN method costs 0.018 s, while the computational time of the traditional solver is close to 0.3 s. Obviously, the LVI-PDNN optimization method also greatly reduces the computational cost.

Remark 2: Theoretically, the traditional dual neural network for dealing with the QP problems has a high computational cost because it requires inverse operation of the matrix (which contains $O(N^3)$ operations). Moreover, per iteration of the dual neural network requires $10N + 4m$ additions/subtractions, $5N(N+m)$ multiplications, an $N+m$ limiter, and $N + m$ integrator operations, while the LVI-PDNN (27) requires performing $5(N+m)$ additions/subtractions, $2(N+m)^2$ multiplications, an $N+m$ limiter, and $N+m$ integrator operations. In the experiment, when N is set to 11 and m is set to 4, the structure and computational complexity of LVI-PDNNs are significantly lower than those of dual neural-network solvers.

IV. Control Design and Stability Analysis

According to (1), the dynamics of the robotic exoskeleton can be converted into the state equations as

$$\dot{x}_1 = x_2 \tag{28}$$

$$\dot{x}_2 = M^{-1}\left[\tau + \tau_e - f_{\text{dis}} - G - Cx_2\right] \tag{29}$$

where $G = M_g + M_v$. Given that the discrete points of the reference trajectory are obtained by the dynamics of the LVI-PDNN algorithms in (27), it is necessary to give the continuous trajectory online and combine the initial desired trajectory to generate a complete reshaped trajectory. Thus, the Bezier curve is utilized to generate a smooth reshaped trajectory. According to [37], the radius of the curvature changes steadily on the Bezier curve, resulting in a continuous reference trajectory x_d^*. Then, we can obtain the desired joint angles q_r^*. The definitions of errors z_1 and z_2 are given as

$$z_1 = x_1 - q_r^* \tag{30}$$

$$z_2 = x_2 - \alpha_1 \tag{31}$$

where α_1 is the virtual control to z_1.

Assumption 1: There exit positive constant vectors $Y_0 = [y_{01}, y_{01}, \ldots, y_{0m}]^T$ and $A_0 = [a_{01}, a_{01}, \ldots, a_{0m}]^T$, satisfying $Y_0 \le A_0 \le k_a$, so that the desired trajectory q_r^* satisfies $-Y_0 \le q_r^* \le Y_0$.

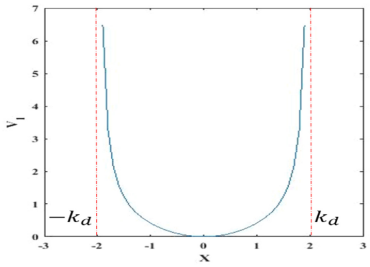

Fig. 3. BLF: $-k_d$ and k_d are the left and right boundary lines of trajectory errors to ensure the safety of manipulators.

Step 1: As shown in Fig. 3, consider a barrier Lyapunov candidate function

$$V_1 = \frac{k_d^2}{\pi}\cot\left(\frac{\pi}{2}\left(1 - \frac{z_1^T z_1}{k_d^2}\right)\right) \tag{32}$$

where $k_d = k_a - Y_0$. The time derivative of V_1 is

$$\dot{V}_1 = \csc^2\left(\frac{\pi}{2}\left(1 - \frac{z_1^T z_1}{k_d^2}\right)\right) z_1^T \dot{z}_1 \tag{33}$$

where

$$\dot{z}_1 = \dot{x}_1 - \dot{q}_r^* = z_2 + \alpha_1 - \dot{q}_r^*. \tag{34}$$

The virtual variable is designed as

$$\alpha_1 = \dot{q}_r^* - A_1 \tag{35}$$

where A_1 is defined as

$$A_1 = \sin^2\left(\frac{\pi}{2}\left(1 - \frac{z_1^T z_1}{k_d^2}\right)\right) K_1 z_1 \tag{36}$$

where $K_1 \in \mathbb{R}^{n\times n}$ and $\lambda_{\min}(K_1) > 0$. Substituting (35) into (34), we have $\dot{z}_1 = z_2 - A_1$, then substituting it into (33), the Lyapunov function is rewritten as

$$\dot{V}_1 = -z_1^T K_1 z_1 + \csc^2\left(\frac{\pi}{2}\left(1 - \frac{z_1^T z_1}{k_d^2}\right)\right) z_1^T z_2. \tag{37}$$

Step 2: The intermediate stability function τ^* should be designed to bound the error z_1 as small as possible. Then, the augmented Lyapunov candidate function can be given as

$$V_2 = V_1 + \frac{1}{2} z_2^T M z_2. \tag{38}$$

Its time derivative yields

$$\dot{V}_2 = \dot{V}_1 + z_2^T M \dot{z}_2 + \frac{1}{2} z_2^T \dot{M} z_2 \tag{39}$$

where

$$\begin{aligned}\dot{z}_2 &= \dot{x}_2 - \dot{\alpha}_1 \\ &= M^{-1}\left[\tau + \tau_e - f_{\text{dis}} - G - Cx_2\right] - \dot{\alpha}_1.\end{aligned} \tag{40}$$

Substituting (37) and (40) into (39) yields

$$\begin{aligned}\dot{V}_2 = &-z_1^T K_1 z_1 + \csc^2\left(\frac{\pi}{2}\left(1 - \frac{z_1^T z_1}{k_d^2}\right)\right) z_1^T z_2 \\ &+ z_2^T(\tau + \tau_e - f_{\text{dis}} - G - C\alpha_1 - M\dot{\alpha}_1).\end{aligned} \tag{41}$$

Given that the parameters of the dynamics are known beforehand, we design the control as

$$\tau^* = -\csc^2\left(\frac{\pi}{2}(1-\frac{z_1^T z_1}{k_d^2})\right)z_1 - K_2 z_2 + f_{\text{dis}} + G + C\alpha_1 + M\dot{\alpha}_1 - \tau_e. \quad (42)$$

Since the disturbance f_{dis} and the exact model of G, C, and M are not available, in addition, the external disturbance can be estimated by including the high-order observer $\hat{f}$ as

$$\tau = -\csc^2\left(\frac{\pi}{2}\left(1-\frac{z_1^T z_1}{k_d^2}\right)\right)z_1 - K_2 z_2 + \hat{W}_D^T S_D(Z_D)\dot{\alpha}_1 + \hat{W}_C^T S_C(Z_C)\alpha_1 + \hat{W}_G^T S_G(Z_G) - K_r \text{sgn}(z_2) + \hat{f} - \tau_e \quad (43)$$

where $K_2, K_r \in \mathbb{R}^{n\times n}$ and $\lambda_{\min}(K_2) > 0, \lambda_{\min}(K_r) > 0$. Specifically, the disturbance observer can be designed as

$$\begin{cases} \hat{f} = \hat{z} - K_d x_2 \\ \dot{\hat{z}} = -K_d \hat{z} + K_d\left(\hat{W}_d^T S_d(Z_d) + K_d x_2\right) \end{cases} \quad (44)$$

where $Z_D = [x_1^T, x_2^T, \alpha_1^T, \dot{\alpha}_1^T], Z_C = [x_1^T, x_2^T, \alpha_1^T, \dot{\alpha}_1^T], Z_G = [x_1^T, x_2^T, \alpha_1^T, \dot{\alpha}_1^T], Z_d = [\tau^T, x_1^T, x_2^T]$, and $K_d^T = K_d > 0$. W_D, W_C, W_G, and W_d are the physical parameters and the updating laws of all NN terms are designed as

$$\dot{\hat{W}}_{Di} = -\Gamma_{Di}(S_{Di}\dot{\alpha}_1 z_{2i} + \theta_{Di}\hat{W}_{Di})(i = 1, 2, \ldots, m) \quad (45)$$

$$\dot{\hat{W}}_{Ci} = -\Gamma_{Ci}(S_{Ci}\alpha_1 z_{2i} + \theta_{Ci}\hat{W}_{Ci})(i = 1, 2, \ldots, m) \quad (46)$$

$$\dot{\hat{W}}_{Gi} = -\Gamma_{Gi}(S_{Gi} z_{2i} + \theta_{Gi}\hat{W}_{Gi})(i = 1, 2, \ldots, m) \quad (47)$$

$$\dot{\hat{W}}_{dk} = -\Gamma_{dk}(K_d S_{dk}\tilde{f}_i + \theta_{dk}\hat{W}_{dk})(k = 1, 2, \ldots, m) \quad (48)$$

where $\Gamma_{Di} > 0; \Gamma_{Ci} > 0; \Gamma_{Gi} > 0; \Gamma_{dk} > 0$; and $\theta_{Di}, \theta_{Ci}, \theta_{Gi}$, and θ_{dk} are positive to improve the robustness. $\hat{W}_D^T S_D(Z_D)$, $\hat{W}_C^T S_C(Z_C)$, and $\hat{W}_G^T S_G(Z_G)$ are the approximation of $W_D^{*T} S_D(Z_D)$, $W_C^{*T} S_C(Z_C)$, and $W_G^{*T} S_G(Z_G)$, respectively, and

$$W_D^{*T} S_D(Z_D) = M + \epsilon_D \quad (49)$$

$$W_C^{*T} S_C(Z_C) = C + \epsilon_C \quad (50)$$

$$W_G^{*T} S_G(Z_G) = G + \epsilon_G. \quad (51)$$

The approximation property of the neural network can also be used to estimate the parameters of the disturbance observer

$$W_d^{*T} S_d(Z_d) = M^{-1}(\tau + \tau_e - Cx_2 - G) - \epsilon_d \quad (52)$$

where W_D^*, W_C^*, W_G^*, and W_d^* are the optimal estimations, and $\epsilon_D, \epsilon_C, \epsilon_G$, and ϵ_d are the estimate errors of each NN term, which satisfy $\max_{Z_D\in\Omega_{Z_D}}|\epsilon_D| < \epsilon_D^*$, $\max_{Z_C\in\Omega_{Z_C}}|\epsilon_C| < \epsilon_C^*$, and $\max_{Z_d\in\Omega_Z}|\epsilon_d| < \epsilon_d^*$, respectively [31].

Theorem 4: Considering the dynamics of the robotic exoskeleton (28) and (29), combining the controller (43), the disturbance observer (44), and the adaptive laws (45)–(48), the control signals of the closed-loop system z_1 z_2, $\tilde{W}_D, \tilde{W}_C, \tilde{W}_G$, and $\tilde{W}_d$ are semiglobally bounded. In addition, the error vectors $z_1, z_2, \tilde{W}_D, \tilde{W}_C, \tilde{W}_G$, and $\tilde{W}_d$ will stay in the compact sets $\Omega_{z_1}, \Omega_{z_2}, \Omega_{\tilde{W}_D}, \Omega_{\tilde{W}_C}, \Omega_{\tilde{W}_G}$, and $\Omega_{\tilde{W}_d}$, respectively, defined as follows: $\Omega_{z_1} = \{z_1 \in \mathbb{R}^n | \ \|z_{1i}\| \le \sqrt{D_1}\}, \Omega_{z_2} = \{z_2 \in \mathbb{R}^n | \ \|z_{2i}\| \le \sqrt{[D_1/(\lambda_{\min}(M))]}\}, \Omega_{\tilde{W}_D} = \{\tilde{W}_D \in \mathbb{R}^n | \ \|\tilde{W}_{Di}\| \le \sqrt{[D_1/(\lambda_{\min}(\Gamma_D^{-1}))]}\}, \Omega_{\tilde{W}_C} = \{\tilde{W}_C \in \mathbb{R}^n | \ \|\tilde{W}_{Ci}\| \le \sqrt{[D_1/(\lambda_{\min}(\Gamma_C^{-1}))]}\}, \Omega_{\tilde{W}_G} = \{\tilde{W}_G \in \mathbb{R}^n | \ \|\tilde{W}_{Gi}\| \le \sqrt{[D_1/(\lambda_{\min}(\Gamma_G^{-1}))]}\}, \Omega_{\tilde{W}_d} = \{\tilde{W}_d \in \mathbb{R}^n | \ \|\tilde{W}_{dk}\| \le \sqrt{[D_1/(\lambda_{\min}(\Gamma_d^{-1}))]}\}$, where $D_1 = 2(V_3(0) + (Z/\kappa))$ with positive definite κ and Z given in (63) and (64). As shown in [41], there is a nonempty initial compact set Ω_i. As long as the initial states $\tilde{W}_i(0), i = D, C, G, d$ start with a given compact set Ω_{i0}, the states $\tilde{W}_i$ will never escape the conservative compact set Ω_i, belonging to the selected compact set $\Omega_{\tilde{W}_i}$, that is, satisfying $\Omega_{i0} \subset \Omega_i \subset \Omega_{\tilde{W}_i}$.

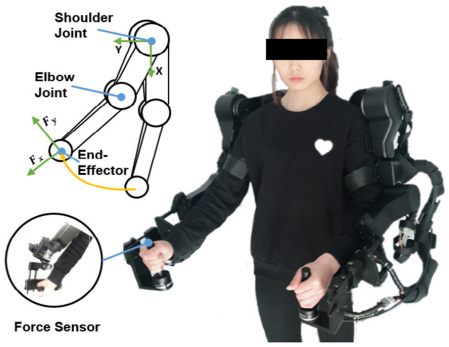

Fig. 4. Experimental interaction system model.

Theorem 5: Considering the robot system described in (1), under Lemma 2, for initial conditions satisfying $z_1(0) \in \Omega_0 := z_1 \in \mathbb{R}^2 : -k_d < z_1 < k_d$, the control law (43) and adaptation law (45)–(48) are adopted. Then, all states of the robot system are semiglobally uniformly bounded, that is, $x_1(t) \longrightarrow q_r^*(t)$ as $t \longrightarrow \infty$. Therefore, the multiple output constraints are all satisfied.

The proof is shown in the Appendix, and the overall control framework for the co-manipulation task is shown in Fig. 2.

V. Experimental Evaluation

A. Experimental Setup

In order to verify the proposed trajectory reshaping and control schemes, the experiments are conducted on the developed dual-arm exoskeleton robot (Fig. 4). Each arm has six DOFs, including two wrist joints, an elbow joint, a shoulder rotation joint, and two shoulder abduction/adduction joints, and its kinematical chain resembles the human's upper limb. These experiments demonstrate how the desired trajectory x_d is adapted with respect to the force f_h applied by the operator. Two motors of the robotic exoskeleton system are equipped as actuators according to the needed torque and the external force in experiments. The motor driver is chosen as Elmo SOL-WHI5/60E01 and the maximum baud rate of CAN bus is 1 Mb/s. In the experiments, the shoulder and elbow joints of the right arm are utilized to assist the subject, and the force sensor installed on the end of the robotic exoskeleton is utilized to measure the interaction force exerted by the subject. Since the measured forces include

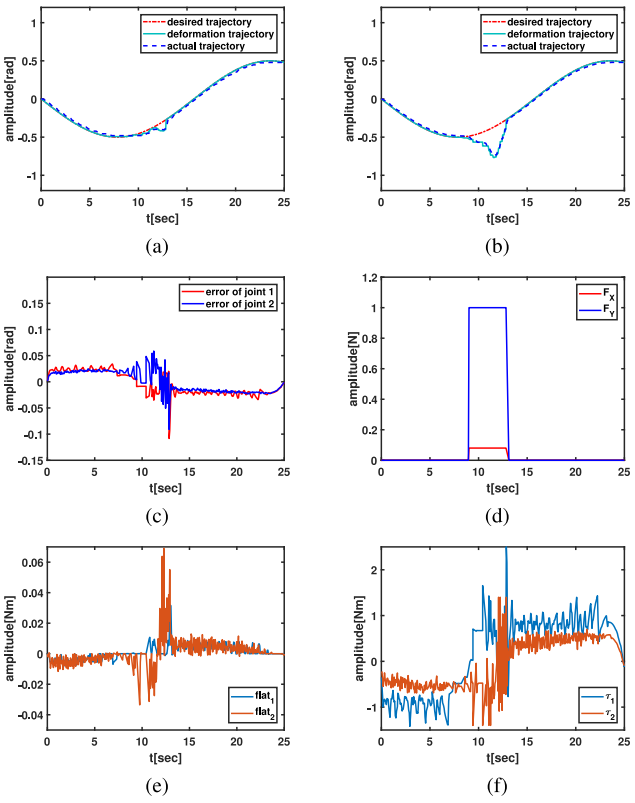

Fig. 5. Experimental results of subject 1. (a) Tracking trajectory of the shoulder joint. (b) Tracking trajectory of the elbow joint. (c) Trajectory error. (d) Interaction force with human f_h. (e) High-order disturbance observer $\hat{f}$. (f) Torque trajectory.

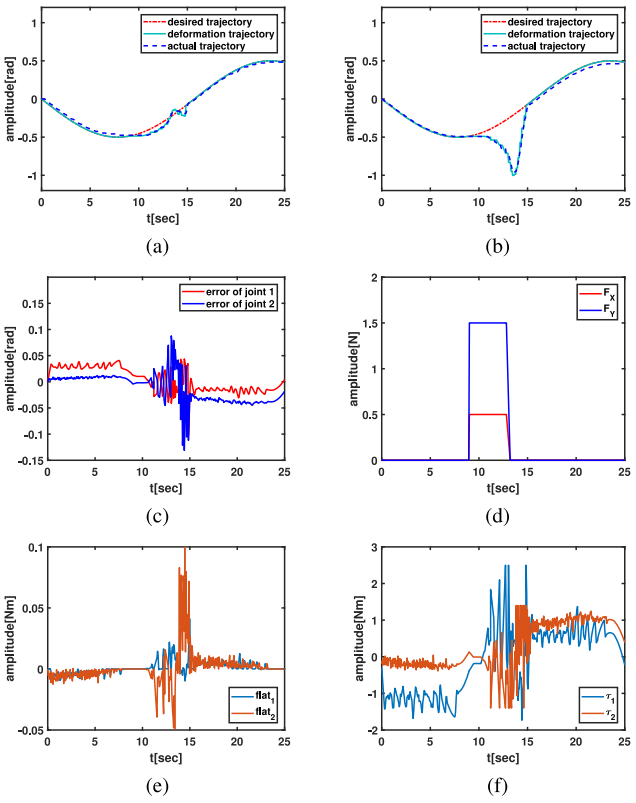

Fig. 6. Experimental results of subject 2. (a) Tracking trajectory of the shoulder joint. (b) Tracking trajectory of the elbow joint. (c) Trajectory error. (d) Interaction force with human f_h. (e) High-order disturbance observer $\hat{f}$. (f) Torque trajectory.

F_x and F_y, the subject and the robot cooperate to complete the specified task in the x–y plane, as illustrated in Fig. 4.

The experiment requires the subject to wear the upper-limb exoskeleton to track a reference trajectory. If the subject does not exert interaction force, the robot drives the subject's limb to follow the predetermined desired trajectory, while in the case of the subject exerting force, the robot needs to follow the human intention trajectory, that is, the reshaped trajectory. According to the developed approach, the experiment mainly involves two partitions, including the utilization of the LVI-PDNN to realize the online optimal reshaping of the trajectory and an adaptive control based on BLF to fulfill tracking of the reconstructed trajectory. To fully validate the feasibility of the proposed strategy, three subjects are involved in the experiment, as shown in Table I. During the experiment, the subject holds the end-effector, and exerts forces in a timely manner to produce the reshaped reference trajectory. For the experiment employed, the subjects have provided the corresponding informed consent, with the approval of the university.

In all experiments, the control gains in (43) are listed in Table II, where λ is designed for scaling the convergence rate of the neural network, k_d is chosen to ensure the safety range, K_2 determines the impedance coefficient, and K_r ensures the robustness of the system. The inputs of each neural network are chosen as $Z_D = [q^T, \dot{q}^T, z_1^T]^T$, $Z_C = [q^T, \dot{q}^T, \ddot{q}^T, z_1^T]^T$, $Z_G = [q^T, \dot{q}^T, z_1^T]^T$, and $Z_d = [q^T, \dot{q}^T, \tau^T]^T$. Since the current of the motor is measurable and proportional to its torque, the input current is used as the control signal to track the desired current.

TABLE I
INFORMATION OF THE SUBJECTS

Experimenter	Age	Weight	Forces	Results
Subject. 1	25 (male)	67.5 kg	Fig. 5d	Fig. 5
Subject. 2	23 (male)	62.1 kg	Fig. 6d	Fig. 6
Subject. 3	24 (female)	46.2 kg	Fig. 7d	Fig. 7

TABLE II
CONTROL PARAMETERS SETTING

Shoulder joint	λ	k_d	K_2	K_r	Γ_{D1}	Γ_{C1}
	50	0.3	3.3	0.3	$0.1I_{64\times64}$	$0.1I_{256\times256}$
	θ_{D1}	θ_{C1}	θ_{G1}	θ_{d1}	Γ_{G1}	Γ_{d1}
	0.5	0.5	0.5	0.2	$0.1I_{64\times64}$	$0.3I_{64\times64}$
Elbow joint	λ	k_d	K_2	K_r	Γ_{D2}	Γ_{C2}
	50	0.3	2.1	0.5	$0.1I_{64\times64}$	$0.1I_{256\times256}$
	θ_{D2}	θ_{C2}	θ_{G2}	θ_{d2}	Γ_{G2}	Γ_{d2}
	0.5	0.5	0.5	0.2	$0.1I_{64\times64}$	$0.3I_{64\times64}$

B. Experimental Results

In order to verify the stability, feasibility, and applicability of the proposed method, we have performed two groups of experiments, involving two different initial desired trajectories. The experimental results of three subjects in the first

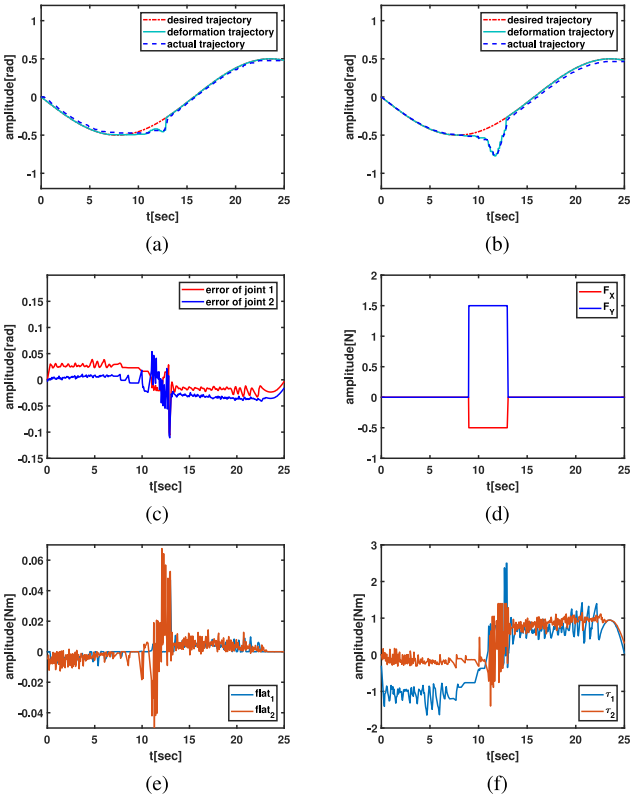

Fig. 7. Experimental results of subject 3. (a) Tracking trajectory of the shoulder joint. (b) Tracking trajectory of the elbow joint. (c) Trajectory error. (d) Interaction force with human f_h. (e) High-order disturbance observer $\hat{f}$. (f) Torque trajectory.

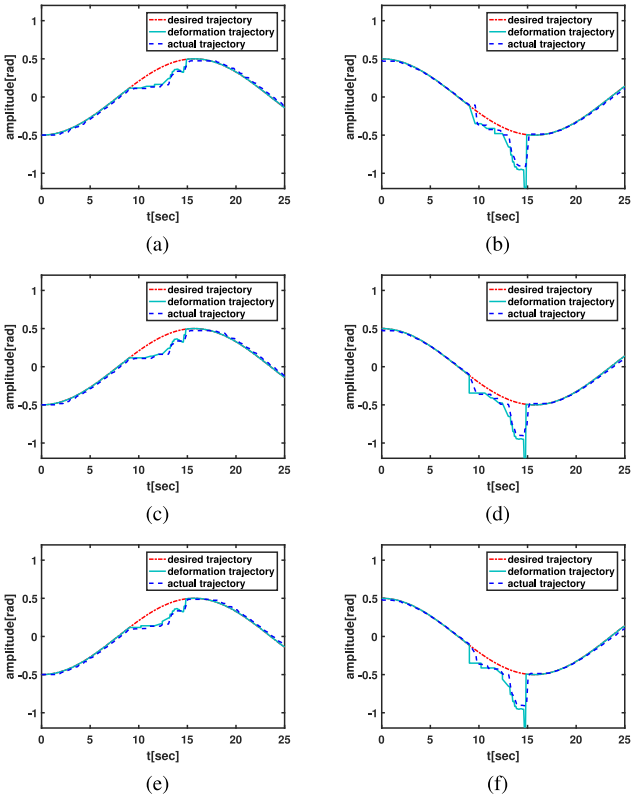

Fig. 9. Experimental results of three subjects under another desired trajectory. (a), (c), and (e) are the shoulder joint's tracking trajectories of three subjects, respectively. (b), (d), and (f) are the elbow joint's tracking trajectories of three subjects, respectively.

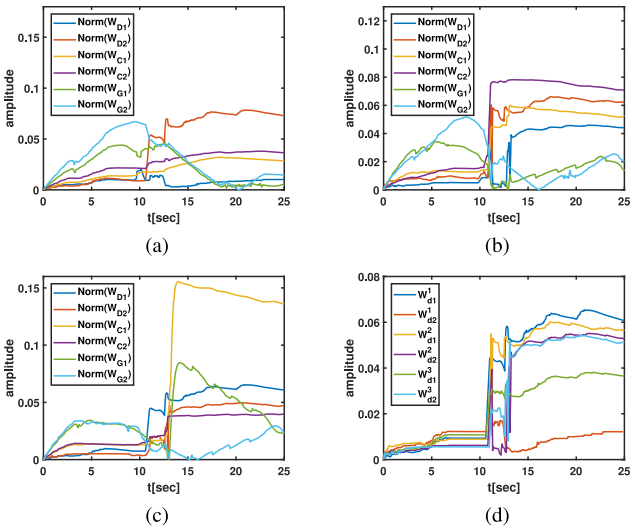

Fig. 8. Neural-network weights. (a) Subject 1. (b) Subject 2. (c) Subject 3. (d) Weights of the neural network in the disturbance observer for three subjects.

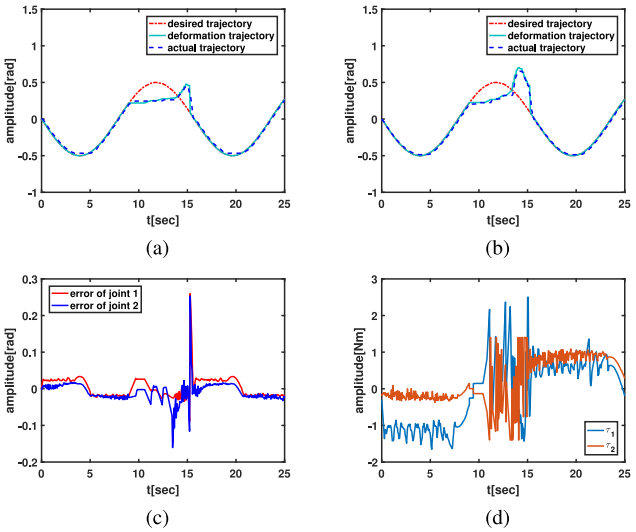

Fig. 10. Experimental results of the subject with the system in higher frequency operation. (a) Tracking trajectory of the shoulder joint. (b) Tracking trajectory of the elbow joint. (c) Trajectory error. (d) Torque trajectory.

initial trajectory are shown in Figs. 5–7, where Figs. 5(a) and (b), 6(a) and (b), and 7(a) and (b) demonstrate the trajectory reshaping and tracking of the shoulder joint (q_1) and the elbow joint (q_2) of three subjects, respectively. Figs. 5(c), 6(c), and 7(c) show the convergence and the boundedness of tracking errors during the experiment; Figs. 5(d), 6(d), and 7(d) show the interaction forces collected by the force sensor; and the estimation of the high-order disturbance observer is shown in Figs. 5(e), 6(e), and 7(e). The weights of each neural network are updated in Fig. 8. Then, the experimental results of three subjects under another initial trajectory are given in Fig. 9. From the experimental results, we can

know that the subject can exert forces on the robot freely, and the robot can produce an optimal and smooth trajectory deformation. When the interaction force disappears, the robot goes back to the desired trajectory, which realizes the shared control between the desired trajectory of the robot and the motion intention of the human. It will contribute to the realization of interactive control between the human and robot in the future. Furthermore, based on the adaptive neural-network control schemes presented in this article, the conflicts between the subject and the robotic exoskeleton gradually decreased with the adaption of the disturbance observer. The reduction of the interaction conflicts demonstrates that the robot exhibits compliance to the human behavior in the co-manipulation task.

Similarly, the applicability of the proposed method in the presence of potential fast motion is also verified by experiments, and the experimental results are shown in Fig. 10, which demonstrate the stability of the system in high-frequency operation, despite a slight increase of the tracking error compared with the low-frequency operation.

VI. Conclusion

In this article, a novel pHRI control design method is proposed, which enables human operators to modify the robot's actual and desired trajectories during the co-manipulation tasks. The developed approach enables human operators to complete collaborative tasks with the robot via physical interactions. Since the reshaped trajectory returns smoothly to the original predetermined desired trajectory without human–robot interaction, the robot can either work autonomously or coordinates with human operators for collaborative tasks. Finally, the experiments are performed on the exoskeleton robot to verify the performance of the developed online trajectory reshaping optimization and control. Future research will consider more interaction tasks to explore the novel methods about estimating human intentions and improving pHRI strategies.

Appendix
Proof of Theorem 4

Reconsidering the Lyapunov function V_2 and substituting the control (43) into (41), we have

$$\begin{aligned}\dot{V}_2 = &-z_1^T K_1 z_1 - z_2^T K_2 z_2 - z_2^T K_r \mathrm{sgn}(z_2) - z_2^T f_{\mathrm{dis}} + z_2^T \hat{f} \\ &+ z_2^T(\tilde{W}_D^T S_D \dot{\alpha}_1 + \tilde{W}_C^T S_C \alpha_1 + \tilde{W}_G^T S_G) + z_2^T \epsilon \end{aligned} \tag{53}$$

where $\epsilon = \epsilon_D \dot{\alpha}_1 + \epsilon_C \alpha_1 + \epsilon_G$. Given $\tilde{W}_D = \hat{W}_D - W_D^*$, $\tilde{W}_C = \hat{W}_C - W_C^*$, $\tilde{W}_G = \hat{W}_G - W_G^*$, and $\tilde{W}_d = \hat{W}_d - W_d^*$, in consideration of the influence of $\tilde{W}_D$, $\tilde{W}_C$, $\tilde{W}_G$, and $\tilde{W}_d$ on the stability of the control system.

Step 3: The control input τ is designed to bound the errors $\tilde{W}_D$, $\tilde{W}_C$, $\tilde{W}_G$, $\tilde{W}_d$, and $\tilde{f}$ as small as possible. Then, the augmented Lyapunov candidate function can be designed as follows:

$$\begin{aligned}V_3 = V_2 &+ \frac{1}{2}\sum_{i=1}^{m} \tilde{W}_{Di}^T \Gamma_{Di}^{-1} \tilde{W}_{Di} + \frac{1}{2}\sum_{i=1}^{m} \tilde{W}_{Ci}^T \Gamma_{Ci}^{-1} \tilde{W}_{Ci} \\ &+ \frac{1}{2}\sum_{i=1}^{m} \tilde{W}_{Gi}^T \Gamma_{Gi}^{-1} \tilde{W}_{Gi} + \frac{1}{2}\sum_{k=1}^{m} \tilde{W}_{dk}^T \Gamma_{dk}^{-1} \tilde{W}_{dk} + \frac{1}{2}\tilde{f}^T \tilde{f}. \end{aligned} \tag{54}$$

Take the time derivative of V_3 and substitute (53) into it

$$\begin{aligned}\dot{V}_3 = \dot{V}_2 &+ \tilde{f}^T \dot{\tilde{f}} + \sum_{i=1}^{m} \tilde{W}_{Di}^T \Gamma_{Di}^{-1} \dot{\tilde{W}}_{Di} + \sum_{i=1}^{m} \tilde{W}_{Ci}^T \Gamma_{Ci}^{-1} \dot{\tilde{W}}_{Ci} \\ &+ \sum_{i=1}^{m} \tilde{W}_{Gi}^T \Gamma_{Gi}^{-1} \dot{\tilde{W}}_{Gi} + \sum_{k=1}^{m} \tilde{W}_{dk}^T \Gamma_{dk}^{-1} \dot{\tilde{W}}_{dk} \end{aligned} \tag{55}$$

where the updating laws are given in (45)–(47), and

$$z_2^T \tilde{W}_D^T S_D \dot{\alpha}_1 = \sum_{i=1}^{m} \tilde{W}_{Di}^T S_{Di} \dot{\alpha}_1 z_{2i} \tag{56}$$

$$z_2^T \tilde{W}_C^T S_C \alpha_1 = \sum_{i=1}^{m} \tilde{W}_{Ci}^T S_{Ci} \alpha_1 z_{2i} \tag{57}$$

$$z_2^T \tilde{W}_G^T S_G = \sum_{i=1}^{m} \tilde{W}_{Gi}^T S_{Gi} z_{2i}. \tag{58}$$

Defining the error of the disturbance observer (44) as $\tilde{f} = \hat{f} - f_{\mathrm{dis}}$, yields

$$\begin{aligned}\dot{\tilde{f}} &= \dot{\hat{f}} - \dot{f}_{\mathrm{dis}} \\ &= -K_d \tilde{f} - K_a f_{\mathrm{dis}} + K_d \tilde{W}_d^T S_d(Z_d) + K_d \epsilon_d - \dot{f}_{\mathrm{dis}} \end{aligned} \tag{59}$$

where $K_a = K_d(I - M^{-1})$. Substituting the updating laws (48) and the disturbance observer error (59) into (55), yields

$$\begin{aligned}\dot{V}_3 = &-z_1^T K_1 z_1 - z_2^T K_2 z_2 - \tilde{f}^T K_d \tilde{f} - z_2^T K_r \mathrm{sgn}(z_2) \\ &+ z_2^T \epsilon + z_2^T \tilde{f} - \tilde{f}^T K_a f_{\mathrm{dis}} + \tilde{f}^T K_d \epsilon_d - \tilde{f}^T \dot{f}_{\mathrm{dis}} \\ &- \sum_{i=1}^{m} \theta_{Di} \tilde{W}_{Di}^T \hat{W}_{Di} - \sum_{i=1}^{m} \theta_{Ci} \tilde{W}_{Ci}^T \hat{W}_{Ci} \\ &- \sum_{i=1}^{m} \theta_{Gi} \tilde{W}_{Gi}^T \hat{W}_{Gi} - \sum_{k=1}^{m} \theta_{dk} W_{dk}^T \hat{W}_{dk}. \end{aligned} \tag{60}$$

Since $-\tilde{W}^T \hat{W} = -\tilde{W}^T(W^* + \tilde{W}) = -\tilde{W}^T \tilde{W} - \tilde{W}^T W^*$ and $-\tilde{W}^T W^* \le (1/2)(\tilde{W}^T \tilde{W} + W^{*T} W^*)$, we have $-\tilde{W}^T \hat{W} \le -(1/2)\tilde{W}^T \tilde{W} + (1/2) W^{*T} W^*$. For stability, the control term K_r is usually selected to be properly large, which can be changed into

$$K_r = \epsilon_D^* \dot{\alpha}_1 + \epsilon_C^* \alpha_1 + \epsilon_G^*. \tag{61}$$

Then, we can obtain $-z_2^T K_r \mathrm{sgn}(z_2) + z_2^T \epsilon < 0$. The chosen gain has several advantages: 1) the values of terms ϵ_D^*, ϵ_C^*, and ϵ_G^* only need to be large enough to compensate for the approximation NN errors ϵ_D, ϵ_C, and ϵ_G, respectively, and 2) it is a function of $\dot{\alpha}_1$ and α_1, which decreases with the decrease of $\dot{\alpha}_1$ and α_1. We have $z_2^T \tilde{f} \le (1/2) z_2^T z_2 + (1/2)\tilde{f}^T \tilde{f}$, $\tilde{f}^T \dot{f}_{\mathrm{dis}} \le (1/2)\tilde{f}^T \tilde{f} + (1/2)||f^*||^2$, $-\tilde{f}^T K_a f_{\mathrm{dis}} \le (1/2)\tilde{f}^T \tilde{f} + (1/2)||K_a||^2 ||f_M^*||^2$, $\tilde{f}^T K_d \epsilon_d \le (1/2)\tilde{f}^T \tilde{f} + (1/2)||K_d||^2 ||\epsilon_d^*||^2$, then substituting these inequalities into (60), yields

$$\begin{aligned}\dot{V}_3 \le &-z_1^T K_1 z_1 - z_2^T (K_2 - 0.5I) z_2 - \tilde{f}^T (K_d - 2I) \tilde{f} \\ &- \frac{1}{2}\left(\sum_{i=1}^{m} \theta_{Di} \tilde{W}_{Di}^T \tilde{W}_{Di} + \sum_{i=1}^{m} \theta_{Ci} \tilde{W}_{Ci}^T \tilde{W}_{Ci} \right. \\ &\left. + \sum_{i=1}^{m} \theta_{Gi} \tilde{W}_{Gi}^T \tilde{W}_{Gi} + \sum_{k=1}^{m} \theta_{dk} \tilde{W}_{dk}^T \tilde{W}_{dk} \right) \end{aligned}$$

$$+\frac{1}{2}\left(\sum_{i=1}^{m}\theta_{Di}W_{Di}^{*T}W_{Di}^{*}+\sum_{i=1}^{m}\theta_{Ci}W_{Ci}^{*T}W_{Ci}^{*}+\sum_{i=1}^{m}\theta_{Gi}W_{Gi}^{*T}W_{Gi}^{*}+\sum_{k=1}^{m}\theta_{dk}W_{dk}^{*T}W_{dk}^{*}\right)+\frac{1}{2}\left(\|f^{*}\|^{2}+\|K_a\|^{2}\|f_M^{*}\|^{2}+\|K_d\|^{2}\|\epsilon_d^{*}\|^{2}\right)\leq-\kappa V_3+Z \tag{62}$$

where

$$\kappa=\min\left(2\lambda_{\min}(K_1),2\lambda_{\min}(K_d-2I),\frac{2\lambda_{\min}(K_2-0.5I)}{\lambda_{\max}(M)}\min_{i=1,2,\ldots,m}\left\{\frac{\theta_{Di}}{\lambda_{\max}(\Gamma_{Di}^{-1})}\right\},\min_{i=1,2,\ldots,m}\left\{\frac{\theta_{Ci}}{\lambda_{\max}(\Gamma_{Ci}^{-1})}\right\}\min_{k=1,2,\ldots,m}\left\{\frac{\theta_{Gi}}{\lambda_{\max}(\Gamma_{Gi}^{-1})}\right\},\min_{k=1,2,\ldots,m}\left\{\frac{\theta_{dk}}{\lambda_{\max}(\Gamma_{dk}^{-1})}\right\}\right) \tag{63}$$

$$Z=\frac{1}{2}\left(\sum_{i=1}^{m}\theta_{Di}W_{Di}^{*T}W_{Di}^{*}+\sum_{i=1}^{m}\theta_{Ci}W_{Ci}^{*T}W_{Ci}^{*}+\sum_{i=1}^{m}\theta_{Gi}W_{Gi}^{*T}W_{Gi}^{*}+\sum_{k=1}^{m}\theta_{dk}W_{dk}^{*T}W_{dk}^{*}\right)+\frac{1}{2}\left(\|f^{*}\|^{2}+\|K_a\|^{2}\|f_M^{*}\|^{2}+\|K_d\|^{2}\|\epsilon_d^{*}\|^{2}\right). \tag{64}$$

To guarantee $\kappa>0$, the design parameters $\theta_{Di}>0,\theta_{Ci}>0,\theta_{Gi}>0,\theta_{dk}>0$, and the control parameters satisfy the following criteria: $K_1=K_1^T>0$ $K_d-2I_{n\times n}=(K_d-2I_{n\times n})^T>0,K_2-0.5I_{n\times n}=(K_2-0.5I_{n\times n})^T>0$. To prove that the signals $z_1,z_2,\tilde{W}_{Di},\tilde{W}_{Ci},\tilde{W}_{Gi}$, and $\tilde{W}_{dk}$ are semiglobally uniformly bounded, we multiply (62) by $e^{\kappa t}$, then

$$\frac{d}{dt}V_3e^{\kappa t}\leq Ze^{\kappa t}. \tag{65}$$

Integrating (62) over $[0,t]$, yields

$$\dot{V}_3\leq(V_3(0)-\frac{Z}{\kappa})e^{-\kappa t}+\frac{Z}{\kappa}\leq V_3(0)+\frac{Z}{\kappa} \tag{66}$$

which implies $V_3(t)$ is bounded according to Lemma 1. From (54) and (66), we can obtain $(1/2)\sum_{i=1}^{n}z_{1i}^2\leq V_3(t)$ and $(1/2)\sum_{i=1}^{n}\lambda_{\min}(M)z_{2i}^2\leq V_3(t)$, so that the error signal $z_{1i},i=1,\ldots,n,\forall t\geq0$ can be uniformly bounded as

$$\frac{1}{2}\|z_1\|^2\leq V_3(0)+\frac{Z}{\kappa} \tag{67}$$

$$\frac{1}{2}\|z_2\|^2\leq\frac{V_3(0)+\frac{Z}{\kappa}}{\lambda_{\min}(M)} \tag{68}$$

and they are ultimately bounded as $\|z_{1i}\|\leq\sqrt{D_1}$ and $\|z_{2i}\|\leq\sqrt{[D_1/\lambda_{\min}(M)]}$, where D_1 has been defined in Theorem 4. According to Lemma 1, the boundedness of $V_3(t)$ guarantees system stability. Letting $V_3(0)+(Z/\kappa)\triangleq b\in\mathbb{R}^+$, then we have $V_3(t)\leq b,\forall t\leq0$. From the definition of BLF $V_3(x)\longrightarrow\infty$ as $|z_1(t)|\rightarrow k_d$ and Lemma 2, it can be seen that the tracking error $z_1(t)$ is kept in the set $z_1\in(-k_d,k_d),\forall t\in[0,+\infty)$, provided that $z_1(0)\in(-k_d,k_d)$. According to Assumption 1, since $x_1(t)=z_1(t)+q_r^*,-Y_0\leq q_r^*\leq Y_0$, and $k_a=k_d+Y_0$, the output constraint is satisfied, that is, $|x_1|\leq k_a,\forall t\geq0$. Hence, the constrained region on the joint space vector is ensured.

REFERENCES

[1] N. Jarrasse *et al.*, "A methodology to quantify alterations in human upper limb movement during co-manipulation with an exoskeleton," *IEEE Trans. Neural Syst. Rehab. Eng.*, vol. 18, no. 4, pp. 389–397, Aug. 2010.

[2] J.-I. Furukawa, T. Noda, T. Teramae, and J. Morimoto, "Human movement modeling to detect biosignal sensor failures for myoelectric assistive robot control," *IEEE Trans. Robot.*, vol. 33, no. 4, pp. 846–857, Aug. 2017.

[3] Y. Mao and S. K. Agrawal, "Design of a cable-driven arm exoskeleton (CAREX) for neural rehabilitation," *IEEE Trans. Robot.*, vol. 28, no. 4, pp. 922–931, Aug. 2012.

[4] J. Huang, W. Huo, W. Xu, S. Mohammed, and Y. Amirat, "Control of upper-limb power-assist exoskeleton using a human–robot interface based on motion intention recognition," *IEEE Trans. Autom. Sci. Eng.*, vol. 12, no. 4, pp. 1257–1270, Oct. 2015.

[5] R. Lu, Z. Li, C.-Y. Su, and A. Xue, "Development and learning control of a human limb with a rehabilitation exoskeleton," *IEEE Trans. Ind. Electron.*, vol. 61, no. 7, pp. 3776–3785, Jul. 2014.

[6] B. Ugurlu, M. Nishimura, K. Hyodo, M. Kawanishi, and T. Narikiyo, "Proof of concept for robot-aided upper limb rehabilitation using disturbance observers," *IEEE Trans. Human–Mach. Syst.*, vol. 45, no. 1, pp. 110–118, Feb. 2015.

[7] A. U. Pehlivan, D. P. Losey, and M. K. O'Malley, "Minimal assist-as-needed controller for upper limb robotic rehabilitation," *IEEE Trans. Robot.*, vol. 32, no. 1, pp. 113–124, Feb. 2016.

[8] T. Teramae, T. Noda, and J. Morimoto, "EMG-based model predictive control for physical human–robot interaction: Application for assist-as-needed control," *IEEE Robot. Autom. Lett.*, vol. 3, no. 1, pp. 210–217, Jan. 2018.

[9] N. Hogan, "Impedance control—An approach to manipulation. I-Theory. II-Implementation. III-Applications," *Trans. ASME J. Dyn. Syst. Meas. Control*, vol. 107, pp. 1–24, Mar. 1985.

[10] S. Jung, T. C. Hsia, and R. G. Bonitz, "Force tracking impedance control of robot manipulator under unknown environment," *IEEE Trans. Control Syst. Technol.*, vol. 12, no. 3, pp. 474–483, May 2004.

[11] A. Suarez, G. Heredia, and A. Ollero, "Physical-virtual impedance control in ultralightweight and compliant dual-arm aerial manipulators," *IEEE Robot. Autom. Lett.*, vol. 3, no. 3, pp. 2553–2560, Jul. 2018.

[12] B. Huang, Z. Li, X. Wu, A. Ajoudani, A. Bicchi, and J. Liu, "Coordination control of a dual-arm exoskeleton robot using human impedance transfer skills," *IEEE Trans. Syst., Man, Cybern., Syst.*, vol. 49, no. 5, pp. 954–963, May 2019.

[13] Z. Li, Y. Kang, Z. Xiao, and W. Song, "Human–robot coordination control of robotic exoskeletons by skill transfers," *IEEE Trans. Ind. Electron.*, vol. 64, no. 6, pp. 5171–5181, Jun. 2017.

[14] Z. Li, Z. Huang, W. He, and C.-Y. Su, "Adaptive impedance control for an upper limb robotic exoskeleton using biological signals," *IEEE Trans. Ind. Electron.*, vol. 64, no. 2, pp. 1664–1674, Feb. 2017.

[15] S. S. Ge, Y. Li, and C. Wang, "Impedance adaptation for optimal robot-environment interaction," *Int. J. Control*, vol. 87, no. 2, pp. 249–263, 2014.

[16] Z. Li, B. Huang, Z. Ye, M. Deng, and C. Yang, "Physical human–robot interaction of a robotic exoskeleton by admittance control," *IEEE Trans. Ind. Electron.*, vol. 65, no. 12, pp. 9614–9624, Dec. 2018.

[17] Z. Li, S. S. Ge, and S. Liu, "Contact-force distribution optimization and control for quadruped robots using both gradient and adaptive neural networks," *IEEE Trans. Neural Netw. Learn. Syst.*, vol. 25, no. 8, pp. 1460–1473, Aug. 2014.

[18] I. Ranatunga, F. L. Lewis, D. O. Popa, and S. M. Tousif, "Adaptive admittance control for human–robot interaction using model reference design and adaptive inverse filtering," *IEEE Trans. Control Syst. Technol.*, vol. 25, no. 1, pp. 278–285, Jan. 2017.

[19] A. Mörtl, M. Lawitzky, A. Kucukyilmaz, M. Sezgin, C. Basdogan, and S. Hirche, "The role of roles: Physical cooperation between humans and robots," *Int. J. Robot. Res.*, vol. 31, no. 13, pp. 1656–1674, 2012.

[20] Y. Li, K. P. Tee, W. L. Chan, R. Yan, Y. Chua, and D. K. Limbu, "Continuous role adaptation for human–robot shared control," *IEEE Trans. Robot.*, vol. 31, no. 3, pp. 672–681, Jun. 2015.

[21] A. Kucukyilmaz, T. M. Sezgin, and C. Basdogan, "Intention recognition for dynamic role exchange in haptic collaboration," *IEEE Trans. Haptics*, vol. 6, no. 1, pp. 58–68, 1st Quart., 2013.

[22] Z. Liu, F. Wang, and Y. Zhang, "Adaptive visual tracking control for manipulator with actuator fuzzy dead-zone constraint and unmodeled dynamic," *IEEE Trans. Syst., Man, Cybern., Syst.*, vol. 45, no. 10, pp. 1301–1312, Oct. 2015.

[23] T. Schmidt, K. Hertkorn, R. Newcombe, Z. Marton, M. Suppa, and D. Fo, "Depth-based tracking with physical constraints for robot manipulation," in *Proc. IEEE Int. Conf. Robot. Autom.*, pp. 119–126, May 2015.
[24] A. Ibeas and M. D. L. Sen, "Robustly stable adaptive control of a tandem of master–slave robotic manipulators with force reaction by using a multiestimation scheme," *IEEE Trans. Syst., Man, Cybern. B, Cybern.*, vol. 36, no. 5, pp. 1162–1179, Oct. 2006.
[25] E. G. Gilbert and I. V. Kolmanovsky, "Nonlinear tracking control in the presence of state and control constraints: A generalized reference governor," *Automatica*, vol. 38, no. 12, pp. 2063–2073, 2002.
[26] W. He, Y. Chen, and Z. Yin, "Adaptive neural network control of an uncertain robot with full-state constraints," *IEEE Trans. Cybern.*, vol. 46, no. 3, pp. 620–629, Mar. 2016.
[27] K. P. Tee, S. S. Ge, and E. H. Tay, "Barrier Lyapunov functions for the control of output-constrained nonlinear systems," *Automatica*, vol. 45, no. 4, pp. 918–927, 2009.
[28] K. P. Tee, B. Ren, and S. S. Ge, "Control of nonlinear systems with timevarying output constraints," *Automatica*, vol. 47, no. 11, pp. 2511–2516, 2011.
[29] K. P. Tee and S. S. Ge, "Control of state-constrained nonlinear systems using integral barrier Lyapunov functionals," in *Proc. IEEE 51st Annu. Conf. Decis. Control*, 2012, pp. 3239–3244.
[30] Z. Li, C. Yang, and L. Fan, *Advanced Control of Wheeled Inverted Pendulum Systems*. London, U.K.: Springer, 2013.
[31] S. S. Ge, C. C. Hang, T. H. Lee, and T. Zhang, *Stable Adaptive Neural Network Control*. Boston, MA, USA: Kluwer, 2001.
[32] S. S. Ge and C. Wang, "Adaptive neural network control of uncertain MIMO non-linear systems," *IEEE Trans. Neural Netw.*, vol. 15, no. 3, pp. 674–692, May 2004.
[33] M. Deng, Z. Li, Y. Kang, C. L. P. Chen, and X. Chu, "A learning-based hierarchical control scheme for an exoskeleton robot in human–robot cooperative manipulation," *IEEE Trans. Cybern.*, to be published.
[34] Y. S. Xia, G. Feng, and J. Wang, "A primal–dual neural network for online resolving constrained kinematic redundancy in robot motion control," *IEEE Trans. Syst., Man, Cybern. B, Cybern.*, vol. 35, no. 1, pp. 54–64, Feb. 2005.
[35] T. Flash and N. Hogan, "The coordination of arm movements: An experimentally confirmed mathematical model," *J. Neurosci.*, vol. 5, no. 7, pp. 1688–1703, 1985.
[36] C. Yang and E. Burdet, "A model of reference trajectory adaptation for interaction with objects of arbitrary shape and impedance," in *Proc. IEEE/RSJ Int. Conf. Intell. Robots Syst.*, San Francisco, CA, USA, 2011, pp. 4121–4126.
[37] K. G. Jolly, R. S. Kumara, and R. Vijayakumar, "A Bezier curve based path planning in a multi-agent robot soccer system without violating the acceleration limits," *Robot. Auton. Syst.*, vol. 57, no. 1, pp. 23–33, 2009.
[38] Y. Zhang, S. S. Ge, and T. H. Lee, "A unified quadratic-programming-based dynamical system approach to joint torque optimization of physically constrained redundant manipulators," *IEEE Trans. Syst., Man, Cybern. B, Cybern.*, vol. 34, no. 5, pp. 2126–2132, Oct. 2004.
[39] Y. Zhang, J. Wang, and Y. Xu, "A dual neural network for bi-criteria kinematic control of redundant manipulators," *IEEE Trans. Robot. Autom.*, vol. 18, no. 6, pp. 923–931, Dec. 2002.
[40] M. Bazaraa, H. Sherali, and C. Shetty, *Nonlinear Programming: Theory and Algorithms*. Hoboken, NJ, USA: Wiley, 1993.
[41] T. P. Zhang and S. S. Ge, "Adaptive neural control of MIMO nonlinear state time-varying delay systems with unknown dead-zones and gain signs," *Automatica*, vol. 43, no. 6, pp. 1021–1033, Jun. 2007.

Xiaoyu Wu received the B.S. degree in automation from Southwest University, Chongqing, China, in 2017. She is currently pursuing the M.S. degree in control engineering with the University of Science and Technology of China, Hefei, China.

Her current research interests include human–robot interaction, motion-control design, and exoskeleton robotics.

Zhijun Li (M'07–SM'09) received the Ph.D. degree in mechatronics from Shanghai Jiaotong University, Shanghai, China, in 2002.

From 2003 to 2005, he was a Postdoctoral Fellow with the Department of Mechanical Engineering and Intelligent Systems, University of Electro-Communications, Tokyo, Japan. From 2005 to 2006, he was a Research Fellow with the Department of Electrical and Computer Engineering, National University of Singapore, Singapore, and Nanyang Technological University, Singapore. Since 2012, he has been a Professor with the College of Automation Science and Engineering, South China University of Technology, Guangzhou, China. Since 2017, he has been a Professor with the Department of Automation, University of Science and Technology, Hefei, China. His current research interests include wearable robotics, teleoperation systems, nonlinear control, and neural-network optimization.

Prof. Li has been the Co-Chair of the IEEE SMC Technical Committee on Bio-mechatronics and Bio-robotics Systems and IEEE-RAS Technical Committee on Neuro-Robotics Systems since 2016. He is serving as an Editor-at-Large for the *Journal of Intelligent and Robotic Systems* and an Associate Editor for several IEEE TRANSACTIONS.

Zhen Kan received the Ph.D. degree in mechanical and aerospace engineering from the University of Florida, Gainesville, FL, USA, in 2011.

He is a Professor with the Department of Automation, University of Science and Technology of China, Hefei, China. He was a Postdoctoral Research Fellow with the Air Force Research Laboratory, Eglin AFB, FL, USA, and the University of Florida REEF, Shalimar, FL, USA, from 2012 to 2016, and an Assistant Professor with the Department of Mechanical Engineering, University of Iowa, Iowa City, IA, USA. His current research interests include networked robotic systems, Lyapunov-based nonlinear control, graph theory, complex networks, and human-assisted estimation, planning, and decision making.

Prof. Kan currently serves as an Associate Editor on the Conference Editorial Board of the IEEE Control Systems Society and Technical Committee for several internationally recognized scientific and engineering conferences.

Hongbo Gao received the Ph.D. degree in computer science and technology from Beihang University, Beijing, China, in 2016.

He is currently an Associate Professor with the Department of Automation, School of Information Science and Technology, University of Science and Technology of China, Hefei, China. He has authored or coauthored over 30 journal papers. He is the co-holder of six patent applications. His current research interests include unmanned system platform and robotics, machine learning, decision support systems, and intelligent driving.